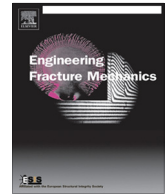




ELSEVIER

Contents lists available at ScienceDirect

Engineering Fracture Mechanics

journal homepage: www.elsevier.com/locate/engfracmech

Stochastic discrete meso-scale simulations of concrete fracture: Comparison to experimental data

Jan Eliáš^{a,*}, Miroslav Vořechovský^a, Jan Skoček^b, Zdeněk P. Bažant^c^a Institute of Structural Mechanics, Faculty of Civil Engineering, Brno University of Technology, Veveří 331/95, Brno 60200, Czech Republic^b HeidelbergCement Technology Center GmbH, Rohrbacher Strasse 95, 69181 Leimen, Germany^c McCormick Institute Professor and W.P. Murphy Professor of Civil Engineering and Materials Science, Northwestern University, 2145 Sheridan Road, CEE/A135, Evanston, IL 60208, USA

ARTICLE INFO

Article history:

Received 4 August 2014

Received in revised form 4 January 2015

Accepted 5 January 2015

Available online 17 January 2015

Keywords:

Discrete model

Lattice-particle models

Energy dissipation

Statistical methods

Size effect

Fracture testing

Notch depth effect

Concrete structures

ABSTRACT

The paper presents a discrete meso-scale model for fracture of concrete taking into account random spatial variability of material parameters. Beams of various sizes, with notches of various depths, are simulated numerically to study the combination of energetic and statistical size effects. A substantial part of material randomness is shown to be caused by random locations of the largest aggregates. Further randomness, due to random fluctuations of material parameters, is considered and an effect of introducing a spatially auto-correlated random field is analyzed. The results of the simulations are compared with recently published experimental data on concrete beams in three-point bending. The differences in the role of randomness in beams of various sizes, with different notch depths, are demonstrated, and differences in energy dissipation are discussed.

© 2015 Elsevier Ltd. All rights reserved.

1. Introduction

The reliability of reinforced concrete structural members is crucial for modern engineering structures. When evaluating the reliability of concrete structures, the fracturing of concrete is one of the crucial phenomena that needs to be included in the analysis. Many features responsible for variability in resistance of concrete can be named. The irregular inner structure of concrete, characterized by random spatial arrangement of grains of various sizes and spatial variability of material properties calls for theoretical model that is able to account for these features. With the help of such a model, the behavior of concrete structures can be studied, understood and predicted, which is needed for design and assessment of engineering structures. The model parameters are usually obtained from small size laboratory specimens, but applying these parameters to large structures poses difficulties. One of them is the spatial randomness of material properties, which is usually insignificant and is ignored for the mean response of small specimens, but becomes significant in large structures.

The need to understand concrete fracture has resulted in the development of complex numerical models that can predict the strength and softening. It is generally agreed that the fracture process in concrete and other quasibrittle materials (ceramics, ice, etc.) is characterized by the gradual release of stress, or softening, within the fracture process zone (FPZ)

* Corresponding author.

E-mail address: elias.j@fce.vutbr.cz (J. Eliáš).

Nomenclature

D	beam depth
S	beam span
b	beam thickness
a_0	notch depth
α_0	relative notch depth
\bar{E}	macroscopic elastic modulus
$\bar{\nu}$	macroscopic Poisson's ratio
E_a	elastic modulus of grains
E_c	elastic modulus of matrix
α	parameter controlling Poisson's ratio
f_t	tensile strength
f_s	shear strength
G_t	fracture energy in tension
G_s	fracture energy in shear
P	loading force
A	area under load–CMOD curve
γ	damage variable
σ_n	nominal stress
g	dissipated energy
l_c	correlation length
\mathbf{H}	random field
$\hat{\mathbf{H}}$	Gaussian random field
\mathbf{x}	spatial coordinate
H	random variable
F_H	cumulative distribution function
Φ	cdf of the standard Gaussian distribution
\mathbf{C}	covariance matrix
ξ	standard Gaussian variable
ρ	correlation
λ	eigenvalue of covariance matrix
ψ	eigenvector of covariance matrix

ahead of the macroscopic crack tip. This gradual softening is understood to be a consequence of concrete heterogeneity. This understanding has led to attempts to include the heterogeneity directly in the material model. Although heterogeneity can be simulated using continuous material description [6], the meso-level simulation of concrete fracture is often performed using discrete models. The simplest and least phenomenological of them are the classical lattice models [14,21,41,26,37,42,38,30], which feature elasto-brittle lattice elements and lattice geometry independent of the material heterogeneity. However, such models require a high resolution, even within the dominant heterogeneities, making them computationally expensive and hence suitable for small specimens only. A reasonable compromise seems to be using a less dense lattice with each node corresponding to one dominant mineral aggregate. Such models may have only translational degrees of freedom and axial connections (i.e., central forces) between grains, as in a truss [4,28,29]. An early model of this kind, efficient enough even for the 1970s computers, was Burton and Dougill's [5] network model, which is recently being emulated by the "peridynamic" models despite the serious inherent limitations of the central force lattice.

A major improvement, making the discrete model much more realistic, was the two-dimensional aggregate interface model [47] in which the particle rotations and interparticle shear interactions were taken into account. This approach was greatly improved and generalized to three dimensions in [8] and recently further refined in the works of Cusatis et al. [10,11]. It is important that his model, called the lattice-particle model, can take into account the three-dimensional rotations of particles or grains, which cause shearing and bending in particle contacts. This can be captured by constitutive law formulated in terms of interface stress and strain vectors, in a way similar to the microplane model. It is a significant advantage that the vectorial constitutive law can directly reflect not only crack opening but also frictional and dilatant slip on plane of distinct orientations. The recent extensions of the lattice-particle model include effects such as chloride diffusion [40,1], fiber reinforcement [31,32] or fatigue [19,13]. A comparison of failure events in the discrete model to acoustic emission measurements during compression test can be found in [27].

The modeling of the fracture process is further complicated by random fluctuations of mechanical properties in concrete. These fluctuations have several sources, among which the randomness in the concrete constituents themselves (material properties, geometric properties), the process by which the constituents are mixed (aggregate locations, non-homogeneous distribution of water, cement, finer aggregates and additives), and non-uniform drying are the most significant. To identify

the material spatial randomness in the form of model stochastic parameters is hard. Moreover, the spatial fluctuations of material properties also complicate identification of parameters for deterministic model because the experimental data are always “contaminated” by the material randomness.

The meso-level models have the advantage of incorporating a substantial part of the randomness through the consideration of the random meso-level structure of the material. To improve the stochastic description of the material, further random fluctuations of model parameters are typically used. Fluctuations are then usually included in the form of a stationary random field [45,17,18]. Each source of randomness naturally has its own characteristic such as the correlation length, probability distribution type, and coefficient of variation.

This paper is focused on two sources of randomness, one resulting from random geometry of the concrete meso-structure which is naturally covered by meso-scale models, and another lumped here into the spatial variation of the material properties described by a random field. The effects of randomness in the model output are investigated from the viewpoint of simulated peak loads, crack patterns and energy dissipation. This paper also tries to address the issue of identification of both the deterministic and stochastic model parameters.

The lattice-particle model (called here *meso-level discrete model*) is here enhanced by random fluctuations to simulate an extensive experimental series of three-point-bend beam tests recently carried out at Northwestern University [24,46]. This series included four different beam sizes (with a size ratio of 1:12.5) and variable notch depths (from no notch at all up to a notch extending to 30% of beam depth). The experiments were controlled by the crack mouth opening displacement (CMOD), to make it possible to measure softening.

Two versions of the model are used in the paper: (i) the full stochastic version and (ii) the original deterministic version with no additional spatial variability in model parameters. By comparing results from the deterministic and stochastic models with the experimental data, one can find what part of the variability in the model response is due to the randomness of grain size and of spatial distribution. The deterministic model is also used to obtain the mean values of model parameters by automatic identification based on matching the peak loads and the areas under the experimental load-CMOD curves. Only the responses of the beams with the deepest notch are used to identify the deterministic model parameters, while the rest of the test data is subsequently compared to the deterministic model predictions. The stochastic parameters unfortunately could not be identified, and were merely generated.

The main objective is to demonstrate the robustness of the model by achieving a good match of the experimental results. Further studied is the influence of specimen size and boundary conditions on the energy dissipation in the model, as well as the effect of additional randomness introduced in the form spatial variability considered in the stochastic model.

2. Model description

The modeling of heterogeneous materials using an assembly of discrete units has become a well established approach with several advantages, such as the relative simplicity and transparency of constitutive law formulation, the ability to represent material heterogeneity, the automatic weakening of the modeled material only in directions perpendicular to cracks, etc. On the other hand, extensive computer resources are often needed to use such models. The present study is based on the three-dimensional (3D) meso-level discrete model developed by [10], which is an extension of [8,9]. The information regarding further development of the model can be found in [11]. Dynamic though the original model is, only the static form of the model is used here.

2.1. Deterministic model

The material is represented by an assembly of ideally rigid 3D cells. The cells are created by a tessellation based on the pseudo-random locations and radii of computer generated spheres, serving as virtual mineral aggregates in concrete. Every cell contains one grain (Fig. 1a and b). The rigid cells are connected through their common facets, on which nonlinear cohesive constitutive law is applied. The damage at the facets then represents the cracking in the matrix and in the interfacial transition zone between two grains. The single damage variable γ controls the loss of material integrity both in the normal and tangential directions of the facet. The evolution of γ depends on the facet strains and the previous loading history (for details, see [10]). The confinement effect, present in the full version of the model, is not implemented here since it is not important for the present problem.

To save computer time, the meso-level discrete model was used only in the regions in which cracking was expected. The other regions of the beams were assumed to remain linearly elastic. They were, therefore, modeled by standard 8-node isoparametric finite elements, which were connected to the meso-level discrete model via auxiliary zero-diameter particles (or nodes) [12]. The macroscopic elastic constants (Poisson's ratio $\bar{\nu}$ and modulus \bar{E}) for the finite elements were identified by fitting a continuous homogeneous displacement field to the displacements of the particle system when both were subjected to a low-level uniaxial compression. In this identification, the inelastic (or fracturing) phenomena are negligible and only elasticity gets manifested.

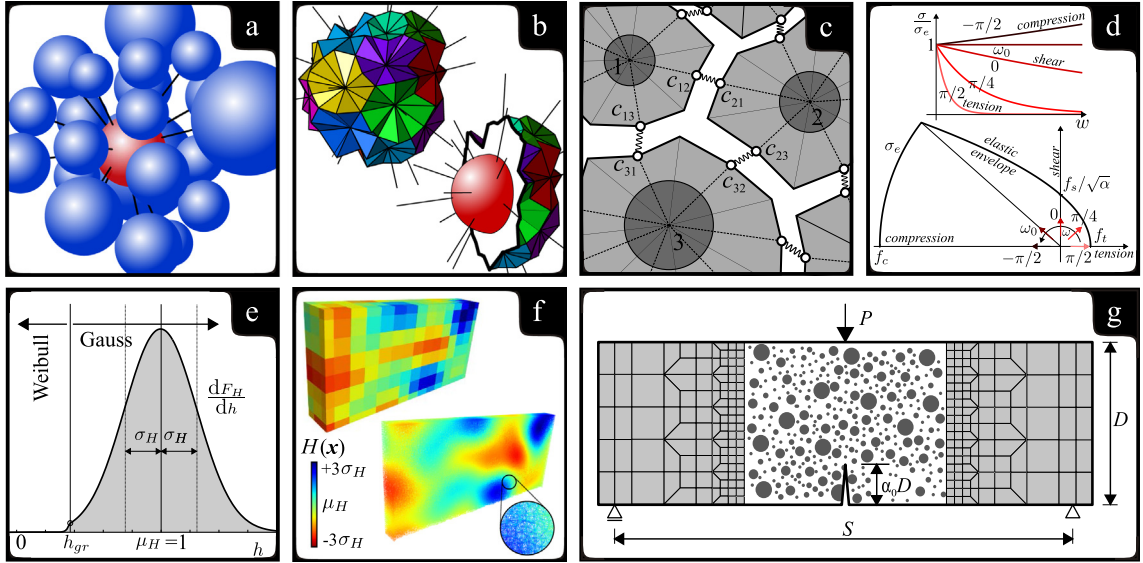


Fig. 1. (a) Concrete meso-structure simulated by the random placement of grains; (b) tessellation providing rigid cells around every grain; (c) contact elements between adjacent cells assumed to lie in the common facet center; (d) constitutive relations assigned to the inter-particle contacts – elastic envelope (bottom) and exponential softening (top), both dependent on the direction of straining [10]; (e) Weibull–Gauss probability distribution used for the randomization of element parameters; (f) random field sample of model parameters generated on a regular grid and projected onto the model elements; (g) specimen shape and boundary conditions.

2.2. Stochastic extension of the model

The only source of the randomness in the original formulation of the model by [10] is in the positioning of grains within the domain. In this paper, we extend the formulation by incorporating random spatial fluctuations in the material properties. At each inter-particle connection, the material parameters are assigned according to a stationary random field $\mathbf{H}(\mathbf{x})$. For a given coordinate \mathbf{x}_0 , $\mathbf{H}(\mathbf{x}_0)$ is a random variable H of the cumulative probability density function (cdf), $F_H(h)$. Since the random field is stationary, the $F_H(h)$ is identical for any position \mathbf{x}_0 .

The strength of quasibrittle structural members is typically governed by the material strength and fracture energy. Realistic fracture models should therefore incorporate the random spatial variability of at least these two variables. The material strength is here considered to be linearly dependent on the fracture energy [17]. Thus, four parameters of the meso-level discrete model—shear strength f_s , fracture energy in shear G_s , tensile strength f_t , and fracture energy in tension G_t —are modeled as mutually linearly dependent. All these random variables share the same distribution and the same coefficient of variation. The same random field is used to generate values for both material strengths and both fracture energies. When any of the four aforementioned mechanical properties are substituted for X , one can write

$$X(\mathbf{x}) = \bar{X}\mathbf{H}(\mathbf{x}) \quad (1)$$

where \bar{X} stands for the mean value of the particular property. The mean value of the (field) random variable H equals 1.

In [3,34,33], it has been shown that the strength distribution of a representative volume element (RVE) of a quasibrittle material should be approximated by a Gaussian (or normal) cdf onto which a remote Weibullian tail is grafted from the left. This Gauss–Weibull distribution is used for our H variable

$$F_H(h) = \begin{cases} r_f \left(1 - e^{-(h/s_1)^m}\right) & h \leq h_{gr} \quad (2) \\ p_{gr} + \frac{r_f}{\delta_G \sqrt{2\pi}} \int_{h_{gr}}^h e^{-\frac{(h-\mu_G)^2}{2\delta_G^2}} dh & h > h_{gr} \quad (3) \end{cases} \quad (2)$$

Here $\langle \cdot \rangle = \max(\cdot, 0)$, $s_1 = s_0 r_f^{1/m}$, m is the Weibull modulus (shape parameter) and s_0 is the scale parameter of the Weibull tail, μ_G and δ_G are the mean value and standard deviation of the Gaussian distribution that describes the Gaussian core and $p_{gr} = F_H(h_{gr})$ is the probability at the grafting point, h_{gr} . The Weibull–Gauss juncture at the grafting point h_{gr} requires equality in the probability density: $(dF_H/dh)|_{h_{gr}^-} = (dF_H/dh)|_{h_{gr}^+}$; r_f is a scaling parameter normalizing the distribution to satisfy the condition $F_H(\infty) = 1$. The distribution has 4 independent parameters in total.

The spatial fluctuation of the field is characterized through an autocorrelation function. It determines the spatial statistical dependence between random variables representing any pair of nodes. The correlation coefficient ρ_{ij} between two random variables at coordinates \mathbf{x}_i and \mathbf{x}_j can be assumed to be a bell-shaped function similar to Gaussian distribution

$$\rho_{ij} = \exp \left[- \left(\frac{\|\mathbf{x}_i - \mathbf{x}_j\|}{l_c} \right)^2 \right] = \prod_{d=1}^{N_d} \exp \left[- \left(\frac{x_{i,d} - x_{j,d}}{l_{c,d}} \right)^2 \right] \quad (4)$$

This form has been selected because the function is differentiable at zero [20] as opposed to the frequently used exponential function (in which power 1 is used instead of 2). Also, the separable correlation function enables the usage of (i) different correlation lengths $l_{c,d}$ along different dimensions d and (ii) a simplified algorithm for the spectral decomposition of a covariance matrix on a regular grid, see Appendix A. In this paper, the autocorrelation length l_c is kept constant in all three directions. A regular grid for discretization of random fields, which enables the usage of EOLE method, is adopted, as described later in this section.

To represent the random field \mathbf{H} of a non-Gaussian variable, H , a commonly used option is to generate an underlying Gaussian random field $\hat{\mathbf{H}}$ and then transform it via the isoprobabilistic (memoryless) transformation

$$\mathbf{H}(\mathbf{x}) = F_H^{-1}(\Phi(\hat{\mathbf{H}}(\mathbf{x}))) \quad (5)$$

where Φ stands for the cdf of the Gaussian field. Such a transformation distorts the correlation structure of the field \mathbf{H} . Thus, when generating the underlying Gaussian field $\hat{\mathbf{H}}$, the correlation coefficients must be modified in order to fulfill the desired pairwise correlations of the non-Gaussian field \mathbf{H} . This is performed using an approximation by the Nataf model [36].

There are several methods of generating a Gaussian random field. Here the Karhunen–Loève expansion is used. It is based on the spectral decomposition of covariance matrix \mathbf{C} (with components $C_{ij} = \rho_{ij}$). It transforms the correlated Gaussian variables $\hat{\mathbf{H}}(\mathbf{x}_i)$ into independent standard Gaussian variables ξ , which are simple to generate. The Gaussian random field is then obtained using vector ξ of K standard Gaussian random variables as follows

$$\hat{\mathbf{H}}(\mathbf{x}) = \sum_{k=1}^K \sqrt{\lambda_k} \xi_k \psi_k(\mathbf{x}) \quad (6)$$

where λ and ψ are the eigenvalues and the eigenvectors of the covariance matrix \mathbf{C} , and K is the number of eigenmodes considered. It is not necessary to use all the eigenmodes of \mathbf{C} . Rather, it suffices to consider only K eigenmodes corresponding to K largest eigenvalues, so that the $\sum_{k=1}^K \lambda_k$ would be about 99% of the trace of the covariance matrix \mathbf{C} [43]. The independent standard Gaussian variables ξ are sampled by Latin Hypercube Sampling using the mean value of each subinterval. The spurious correlation of these variables is then minimized by reordering their realizations during a simulated annealing optimization process [44].

The realizations of the random field need to be evaluated at every shared facet center of the meso-level discrete model. This can be computationally demanding for a large number of facets, because the covariance matrix is then large as well. In the present simulation, there may be about 200,000 inter-particle connections. To overcome this computational burden, the expansion-optimal linear estimation method (EOLE [35]), is adopted. This method significantly reduces the time required for random field generation. The field is initially generated on a regular grid of nodes with spacing $l_c/3$ (see Fig. 1f) instead of at the facet centers. The values of the random field at the model facets are then obtained from the expression

$$\hat{\mathbf{H}}(\mathbf{x}) = \sum_{k=1}^K \frac{\xi_k}{\sqrt{\lambda_k}} \psi_k^T \mathbf{C}_{xg} \quad (7)$$

where λ and ψ are the eigenvalues and eigenvectors of the covariance matrix of the grid nodes; \mathbf{C}_{xg} is a vector of covariances between the facet center at coordinates \mathbf{x} and the grid nodes; and ξ_k are independent standard normal variables. After the Gaussian random field values at facet centers are obtained by EOLE (Eq. (7)), they need to be transformed to non-Gaussian space by Eq. (5).

Besides significant time savings, another advantage of using EOLE is that one can simply use the same field realization for several different granular positions. By keeping realizations of the decomposed independent variables ξ , the field realization can be adapted for any configuration of the facets in the meso-level discrete model. This feature will be used later. The random field realizations on a grid will be generated only once (24 realizations for every correlation length) and these grid random fields will be used repetitively for every beam geometry.

3. Experimental series and identification of model parameters

The experiments were performed at Northwestern University by Hoover et al. [24,22]. Beams with and without a notch were loaded in three-point-bending; the tests were controlled via CMOD, which ensures stable crack propagation and thus allow us to obtain postpeak softening. The series contained beams of four different depths $D = 500, 215, 93$ and 40 mm, geometrically similar in two dimensions. They are labeled by the capital letters, A, B, C and D, respectively. The thickness $b = 40$ mm was the same for all the specimens and the span was $2.176D$. Five notch depths were tested: $\alpha_0 = a_0/D = 0.3, 0.15, 0.075, 0.025$ and 0. These are denoted by the lower-case letters a ($\alpha_0 = 0.3$), b, c, d and e ($\alpha_0 = 0$). Between 6 and 12 experiments were performed for all the size-notch depths combinations except for geometries Cb and Db, which were not suitable for testing.

Identification of the material parameters in the numerical model is based on simple minimization of the difference between the experimentally measured and simulated responses. No attempt has been made to estimate the model parameters from information about the concrete mix composition. The grain diameters were considered to be distributed according to the Fuller curve. The maximum grain size was set to 10 mm according to the aggregates in the tested material. The grains with diameter below 2 mm were not modeled directly, since they were regarded as an integral part of the matrix.

3.1. Identification of deterministic parameters

In the first step of identification, only the deterministic parameters were found. The constitutive law of the deterministic model has several parameters related to different failure modes (the compressive strength and compressive hardening) or parameters hard to identify from the available limited set of experiments (the shear strength and shear fracture energy, the asymptote of the hyperbolic elastic envelope). Values of these parameters were taken from the original paper [10]. Only four free parameters were considered for identification: the elastic modulus of the matrix E_c , parameter α determining the macroscopic Poisson's ratio, tensile strength f_t and fracture energy in tension G_t . The remaining parameters were considered (based on [10]) to be as follows: elastic modulus of grains $E_a = 3E_c$, shear strength $f_s = 3f_t$, shear fracture energy $G_s = 16G_t$, compressive strength $f_c = 16f_t$, initial slope of compressive hardening $K_c = 0.26E_c$, asymptotic slope of the hyperbola determining the elastic limit in tension and shear $\mu = 0.2$, compressive hardening parameter $n_c = 2$, and parameter of compressive elastic envelope $\beta = 1$.

To identify the deterministic parameters, only the responses of beams with the deepest notch (Aa, Ba, Ca, Da) were used. There are two reasons for limiting the identification process to the deepest notch only: (i) the presence of a strong stress concentration induced by a deep notch minimizes the effect of spatial randomness on the mean response [15,16] and (ii) simulating the remaining beam geometries and comparing the results to the experimental data that have not been used in the identification process reveals whether the model can provide reasonable predictions.

The macroscopic elastic parameters (used for the surrounding finite elements) were estimated first. The Poisson's ratio for concrete is usually approximately $\bar{\nu} \approx 0.19$. By trial-error fitting of the elastic part of the load-CMOD curves, the macroscopic elastic modulus was found to be $\bar{E} \approx 36.5$ GPa. By fitting a continuous homogeneous displacement field to the displacements of the particle system when both were subjected to low-level uniaxial compression, the corresponding meso-level discrete model parameters were identified: $E_c = 25$ GPa and $\alpha = 0.29$.

The tensile strength and fracture energy were identified via the simple automatic minimization of the maximum relative difference between the measured and simulated peak loads and the areas under the load-CMOD curves. The mean experimentally measured maximal load, \bar{P}^{exp} , and the area under the load-CMOD curve up to an opening of 0.15 mm, \bar{A}^{exp} , represented the values that should be closely reproduced. The corresponding simulated values ($P^{\text{sim}}, A^{\text{sim}}$) were evaluated for every iteration of the optimization algorithm. The error to minimize was calculated as

$$\max \left(\frac{|\bar{A}_c^{\text{exp}} - A_c^{\text{sim}}|}{\bar{A}_c^{\text{exp}}}, \frac{|\bar{P}_c^{\text{exp}} - P_c^{\text{sim}}|}{\bar{P}_c^{\text{exp}}} \right) \text{ for } c \in \{Aa, Ba, Ca, Da\} \quad (8)$$

The simulated quantities A^{sim} and P^{sim} were obtained using the deterministic model with one (constant) grain position only. For more reliable identification, one should perform several simulations with different grain positions for every evaluation of the objective function. The optimization process is shown in Fig. 2. The minimum achieved error was 0.067 (6.7%).

3.2. Identification of stochastic parameters

In the second identification step, at least some of the stochastic parameters were expected to be identified. It was presumed that the coefficient of variation of \mathbf{H} could be determined from the deep notch results. As shown in [15,16], the spatial fluctuations of local strengths and fracture energies have a negligible effect on the response if the crack initiates from a deep

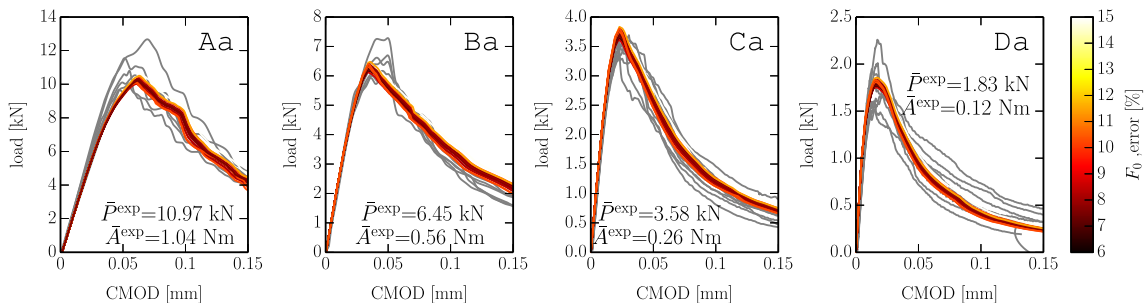


Fig. 2. Comparison of experimental load-CMOD curves and simulated responses obtained by automatic optimization.

notch. The only values that matter are the random parameters located close to the notch tip, which are directed solely by distribution F_H and not by the correlation length.

Therefore, one can separate the local properties of the randomness (distribution F_H) from the spatial properties (correlation length l_c) by introducing a strong stress concentrator. Consequently, by matching the variability of experimental responses for a deep notch, it is possible to estimate the coefficient of variation of the random field. Once this was done, one should be able to identify the correlation length by matching the peak loads of the unnotched beams. As shown in the aforementioned papers [15,16], the mean value of the peak load of unnotched beams strongly depends on the correlation length.

Unfortunately, this theoretical procedure could not be applied in the current study for two reasons. First, the experimental scatter for deep notch beams was already very close to the statistical scatter of the deterministic model, where the randomness is generated only by the random locations of grains. The coefficient of variation of H would thus have to be considered close to zero. Second, introducing randomness into no-notch simulation can only lead to a decrease in the mean peak loads, but the deterministic model for no-notch beams already exhibited lower peak loads than those measured experimentally.

This observation suggests that any randomness other than that caused by the locations of the largest aggregates was negligible in these tests. Therefore, it was decided that the variability present in the deterministic model is sufficient for reproducing the randomness in the experimental series. Instead of using the random field to achieve a closer fit of the measured data, the numerical analysis was run with an artificial excessive coefficient of variation (0.25) in order to study the effect of model randomness deeper.

The following parameters of the distribution F_H were used: Weibull modulus $m = 24$; $s_1 = 0.486$ MPa; grafting point $h_{gr} = 0.364$ MPa; standard deviation of the Gaussian core $\delta_c = 0.25$ MPa. These parameters provided the overall mean value $\mu_H \approx 1$; standard deviation $\delta_H \approx 0.25$, and grafting probability $F_H(h_{gr}) \approx 10^{-3}$. The selection of grafting probability was based on recommendations in [3] where it has been found that the grafting point should be at probabilities between 10^{-5} and 10^{-2} , and most likely around 10^{-3} .

Two correlation lengths l_c were considered: a shorter length, $l_c = 40$ mm (as found in [17]), and a longer length, $l_c = 80$ mm (as found in [45]).

4. Deterministic modeling

All the experimental beam geometries were modeled using the deterministic parameters identified from the deeply notched beams. Ten simulations, differing in the random locations of grains, were performed for each geometry. The self-weight was applied in the first step. In the following steps, the external load P was calculated to gain a stable increase in CMOD. The lengths of CMOD increments were adjusted to keep the number of iterations per step reasonable.

The CMOD control cannot be applied to beams with a shallow or zero notch, because the crack location is not known in advance. In such a case, several openings were measured over several short intervals along the beam span and the simulation was controlled by the largest of these openings. Because there was no gap between the intervals, the crack had to initiate inside one of them, and the CMOD could thus be obtained. This is, however, barely possible in real experiments. Therefore, the experimental opening was measured by one gauge over only a finite, not too long, base length, with the hope that the crack would occur inside that base length. The corresponding gauge opening was extracted from the simulations, too, in order to compare it with the experiments.

It is worth mentioning that it is nearly impossible to simulate smaller beams with the present model. The specimen of size \mathbb{D} has the depth of $4 \times$ the maximum grain diameter and the lattice representing the concrete material is already too coarse. It might also be hard to simulate larger unnotched specimens. The model of geometry \mathbb{Ae} has approximately 300 thousands degrees of freedom and, when only one processor is used, it takes about a week to calculate the response.

The responses of the experiments and the model are compared in Fig. 3. The vertical axis measures the nominal stress defined as

$$\bar{\sigma}_n = \frac{3PDS}{2bD^3} = \frac{3.264P}{bD} \quad (9)$$

where the superior bar above σ means that the nominal stress was evaluated using the nominal beam dimensions, rather than the real dimensions measured on each specimen separately. The horizontal axis shows the elongation measured along the bottom surface over a distance corresponding to the gauge length used in experiments [46]. Each subgraph has the mean value and standard deviation of nominal strength plotted in its top right corner; the number at the same position gives the relative difference between the mean nominal strengths of the model and the experiment. The simulations were terminated as soon as the loading force decreased below 30% of its maximum value. As mentioned, the material identification was performed for the leftmost column only; all the other columns are model predictions. The agreement with tests appears to be satisfactory. Nevertheless, some problems are present:

- The model underestimates the peak loads for most, but not all beam geometries. This indicates that the identification is not ideal. Consideration of other beam geometries for identification would improve the performance of the model, but the illustration of the predictive capabilities of the model would be lost.

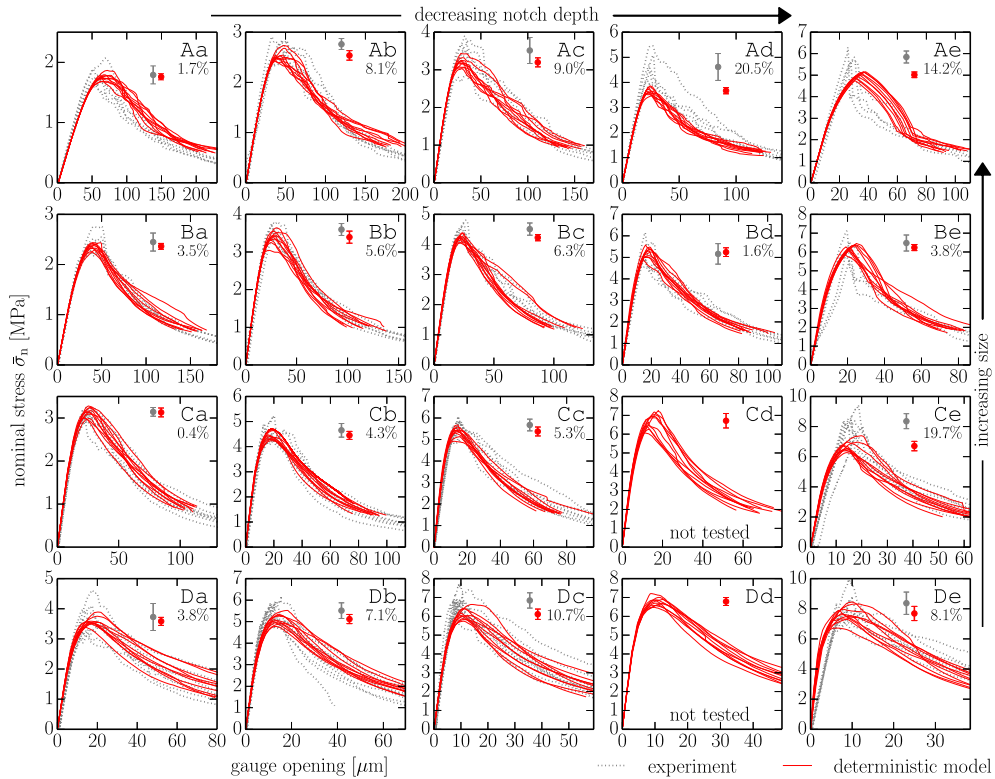


Fig. 3. Responses obtained by the deterministic model compared to the responses recorded during experiments.

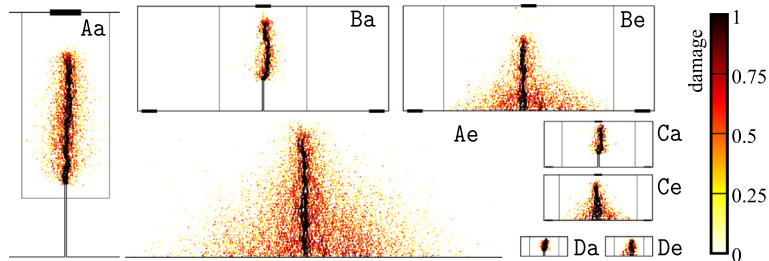


Fig. 4. Some damage patterns obtained by the deterministic meso-level discrete model.

- The elastic parts of the experimental and model responses significantly differ for the smallest geometry D_e . The reason appears to be that the underlying lattice of inter-particle contacts in such small specimens is inevitably too coarse, and also that the response is affected by the regions with biased tessellation closer to the boundaries occupying a large portion of the specimen.
- The two largest unnotched specimens (A_e and B_e) had convergence problems right after the peak, which can be attributed to a sudden strong snap-back present in the load-deflection curve.

Fig. 4 shows some damage patterns obtained by the deterministic model. One can see that the no-notch simulations produce a wide zone of distributed micro-cracking, which develops prior to reaching the peak load. However, after the localization that develops at the peak load, the crack looks about the same as in the case of deeply notched specimens. Another interesting point is the dependence of the damage zone width on the specimen size, which is clearly visible for the deeply notched beams. The larger the specimen, the wider the damaged area. This feature was previously reported in [12,15].

5. Effects of spatial randomness

The application of additional spatial randomness is not meant to bring the results of the model closer to those obtained in experiments. It is performed here in order to study the effects of randomness on the model behavior.

For every geometry and every correlation length, 24 simulations were performed differing in both random grain positions and random field realizations. However, the 24 random field realizations for each geometry were obtained from the same 24 grid realizations by using each realization repetitively. The resulting load-gauge opening curves are plotted in Fig. 5, along with the means and standard deviations of the peak loads in the upper right corner of every subplot.

The notches too shallow compared to the aggregate size induce weak stress concentrations, which nevertheless suffice, in most cases, to force the crack to start from the notch tip. However, it may happen that, due to randomness, a crack initiates outside the shallow notch at midspan. The crack in unnotched beams may initiate away from the midspan as well. If the gauge length is too small, the crack may even initiate outside of the gauge length, and then the gauge gradually closes during the softening regime. This is why some of the responses for \bar{d} and \bar{e} beams exhibit decreasing gauge opening after reaching the peak load. Nevertheless, the convergence problems in the unnotched beams are not as severe as they are in the deterministic analysis. This is explained by the additional randomness which helps to localize the crack.

Fig. 6 shows the size effect plots of nominal strength using Eq. (9) and the maximum load P^{\max} . The nominal strengths from experiments are taken directly from [24]. They are calculated using real dimensions measured directly on specimens, which varied slightly. The deterministic model parameters were optimized using the nominal dimensions, but even after filtering out the geometrical differences among the test specimens using their real dimensions, the correspondence between the experimental data and the deterministic model prediction is acceptable.

For the deeply notched specimens, the application of the additional randomness leads only to an increase in the variance of response. The average peak load does not change, compared to the deterministic model. The observed increase in variance appears more or less independent of the correlation length. It was planned to use this expected behavior to identify the coefficient of variation of H .

A different situation arises for the unnotched specimens. In contrast to the deeply-notched specimens where the crack always starts to propagate from the notch tip, the unnotched specimens are free of any stress concentrator, allowing the macro-crack to initiate at the bottom face even far from the midspan. The region with the worst random combination of stress and local strength will serve as an initiation point. The larger the area where the crack may initiate and the shorter the correlation length, the weaker the local strength that may appear. One can thus see that the difference between the deterministic and stochastic peak loads increases with increasing size and decreasing correlation length.

Several elected damage patterns obtained with the stochastic model ($l_c = 40$ mm) are shown in Fig. 7. Only one grid realization of the random field, applied to different beam geometries, is shown. The large zone of distributed cracking prior to the peak load, which was present in deterministic simulations of unnotched beams, is reduced. The pre-peak cracking is already localized into weaker regions only. Geometry B \bar{a} shows a crack initiated outside the shallow notch.

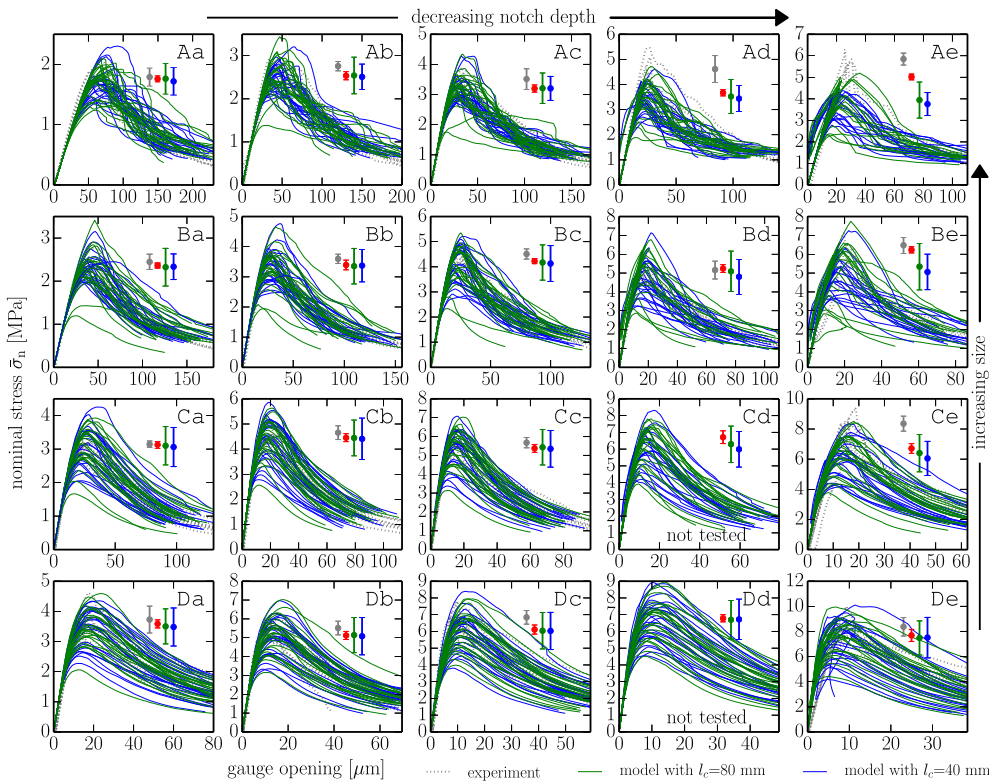


Fig. 5. Responses obtained by the stochastic model (for two different correlation lengths) compared to the responses recorded during experiments.

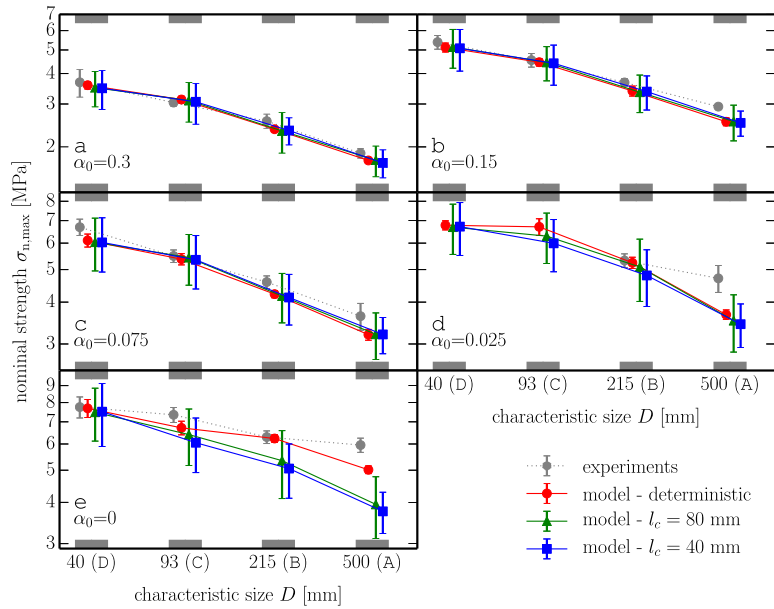


Fig. 6. Size effect plots comparing nominal strengths measured in experiments and calculated by models.

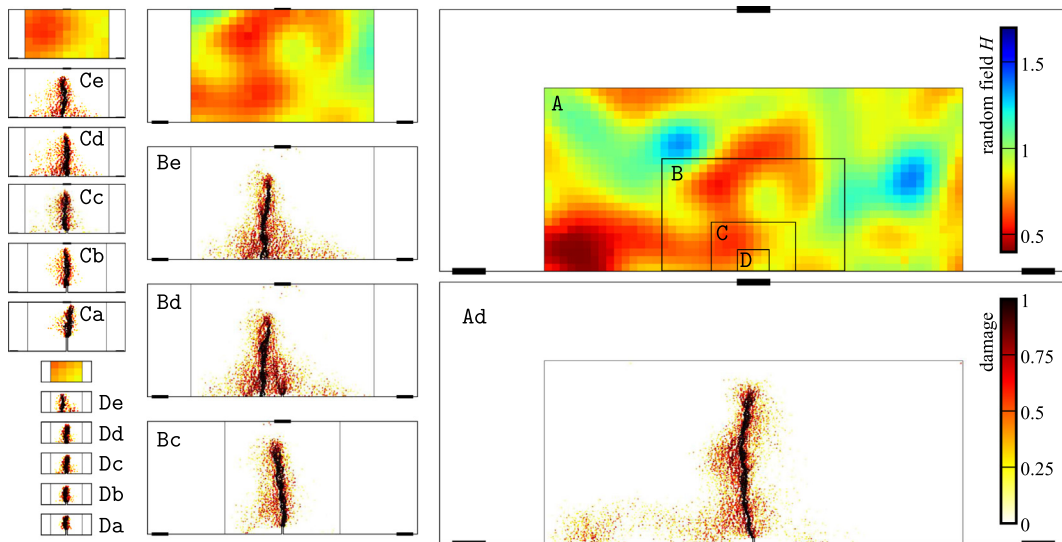


Fig. 7. Some damage patterns obtained by the stochastic meso-level discrete model for different geometries but the same realization of the random field.

Fig. 8 documents the positions of macro-cracks at the bottom face measured in the experiments [46] and obtained in the deterministic and both stochastic models. The two deepest notches, a and b, led to initiation from the notch tip in all simulations and also in all experiments; they are therefore excluded from the figure. In the case of shallow notches c and d, experiments and the deterministic simulation also led to initiation of the macro-crack from the notch tip in all cases.

The stochastic simulations for these too shallow notches may lead to crack initiation outside the notch; however, this occurs only rarely, in spite of the large variability and shallowness of the notches considered. One would expect fewer cracks outside the shallow notch for smaller beams because the chance for a crack to start outside the notch is now restricted by very short spans and thus weaker random field fluctuations. But this is true only for the smallest size D , for which the random field fluctuations are almost suppressed. Regarding other beam sizes, the initiation of a crack outside the notch is more frequent in smaller beams. In these cases, the only value that matters is the absolute, rather than relative, notch depth. As the specimen size decreases, the absolute notch depth decreases as well, and its stress concentration becomes less important

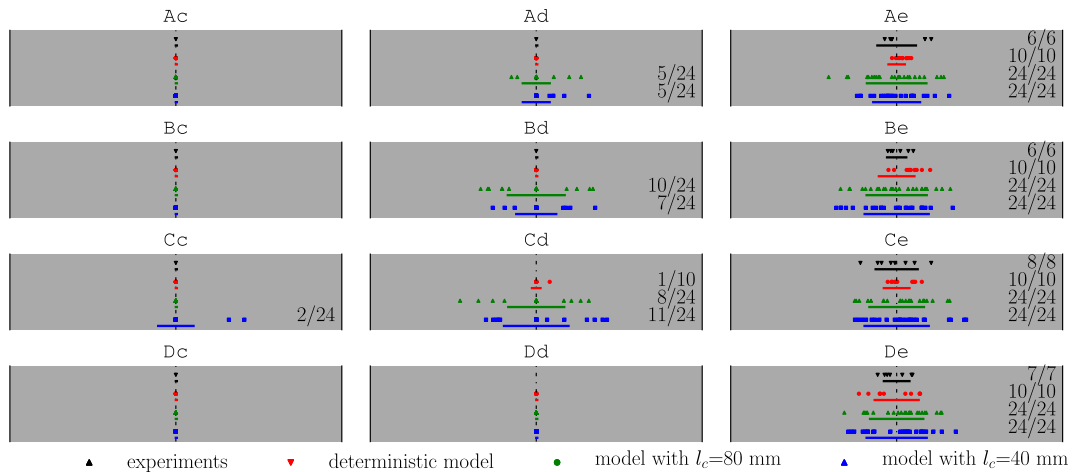


Fig. 8. The horizontal position of the macrocrack in the bottommost layer is shown by a separate marker for each simulation/experiment. The beam span is scaled to constant length; the horizontal positions of supports are marked by black vertical lines, and a dash-and-dot line shows the midspan. The colorful horizontal lines below the markers show \pm standard deviation (assuming the mean value is at the midspan) of the horizontal position of the macrocrack. Numbers display the quantity of cracks outside the notch and the total number of simulations.

compared to the stress disturbances due to material heterogeneity. This facilitates crack initiation at locations other than at the notch tip.

Fig. 8 also shows the crack positions obtained in the unnotched beam models. The relative interval in which the cracks occurred increased after the application of randomness, but it seems to be about the same for both correlation lengths and all the beam sizes. The comparison to experimental data is difficult, due to the limited number of experiments, but the variability in crack position measured in experiments is similar to the results of the deterministic model rather than to the results of the stochastic models.

6. Analysis of energy dissipation

The energy dissipation during fracturing is examined via the dissipated energy per unit area at a specific beam depth, g . This energy is calculated by summing the energies G_i dissipated at individual contacts, i , within a horizontal strip of width 2τ . One selects all the elements i at depth $y_i \in (y - \tau, y + \tau)$, and then sums their energies released since the beginning of the simulation. The summation is then normalized by specimen thickness b and strip width 2τ

$$g(y) = \sum_{i: |y_i - y| \leq \tau} \frac{G_i}{2b\tau} \tag{10}$$

Fig. 9 shows the energy variable g at the peak load along the specimen depth, for all the beam geometries. Deterministic simulations are shown on the left hand side, whereas the right hand side displays the stochastic results. The mean value (bold line) and standard deviation (shaded area) of g were evaluated from 10 deterministic or 24 stochastic realizations. The strip width was chosen to be the same as the maximum grain size, i.e. $2\tau = 10$ mm. The consecutive strips were always placed so that the notch tip would be located at the beginning of the first strips.

Except for an increased standard deviation, there is no difference between the stochastic and deterministic results when the notch is present. But the unnotched beams exhibit, in the case of deterministic modeling, a large area of distributed cracking prior to reaching the peak load. This area is visible in the graph as an increased energy dissipation close to the bottom surface. The stochastic model lacks the distributed cracking because the pre-peak cracking is already localized into weak regions only. Therefore, no increase in g can be seen for unnotched stochastic beams. Comparing the stochastic models with two different correlation lengths, the figure shows a slightly larger dissipation for a longer correlation length in the unnotched case, while for the notched beams the situation is opposite.

There is a clear dependence of g on the specimen size. This is attributed to the increasing stress gradient that constrains the development of the fracture process zone for a decreasing beam size. The lower the constraint, the more the crack branches in the model. One can also see that the maximum value of g (located above the notch tip) decreases with decreasing notch depth.

As the simulation continues, the crack localizes and propagates. Fig. 10 shows g at the end of the simulation. A stress-free crack is seen to develop in the bottom zone of the beam, and so g should have reached its *final* value and might be considered to be equal to the macroscopic mode-I fracture energy.

- Smaller beams have smaller *final* values of g . This is again caused by the increasing stress gradient that constrains the fracture process zone for decreasing size.

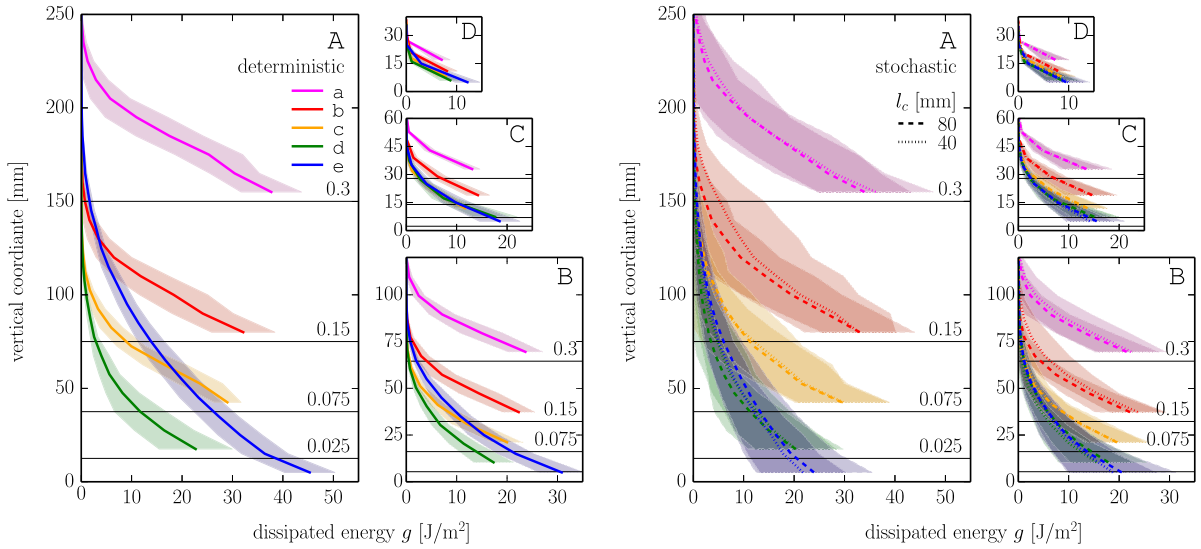


Fig. 9. Energies g dissipated at specific beam depths until the maximum load was reached. The thick line refers to the average value and the shaded area shows standard deviation. Left: deterministic model; right: stochastic models with correlation length $l_c = 40$ and 80 mm.

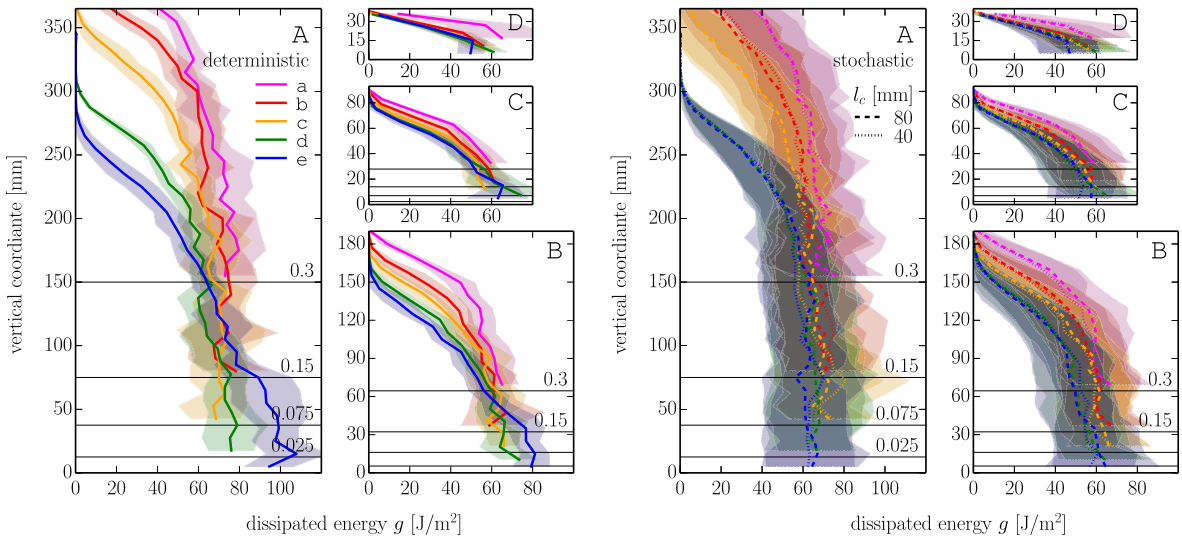


Fig. 10. Energies g dissipated at specific beam depths until the termination of the simulations.

- Although the *final* value of g for notched beams is about the same irrespective of notch depth, it was shown in [12] that it may significantly decrease for extreme notch depths of $\alpha_0 \geq 0.7$.
- In the upper parts of the graphs in Figs. 9 and 10, g decreases rapidly from its more or less constant *final* value because the simulation was stopped before the stress-free crack reached this depth; i.e. g had not reached its *final* value yet.

Fig. 10 shows once again how the randomness affects the energy dissipation. As in Fig. 9, the added randomness also only increases the energy dissipation variance with no effect on its mean value. The only exception is the unnotched beam, due to the previously discussed pre-peak distributed cracking.

The presently observed dependency of the energy dissipation on the specimen size and depth appears to support the frequently expressed idea that macroscopic fracture energy of heterogeneous quasibrittle material is not constant. However, the differences in the average dissipated energy (*final* value of g) in small and large specimens are rather small. Therefore, it can be concluded that, for the size range analyzed, the macroscopic fracture energy for cohesive crack (crack band) model could be considered approximately constant. This was recently shown for the same experimental series analyzed using continuous finite elements with constant fracture energy as a material parameter [23]. It was shown that an excellent match of

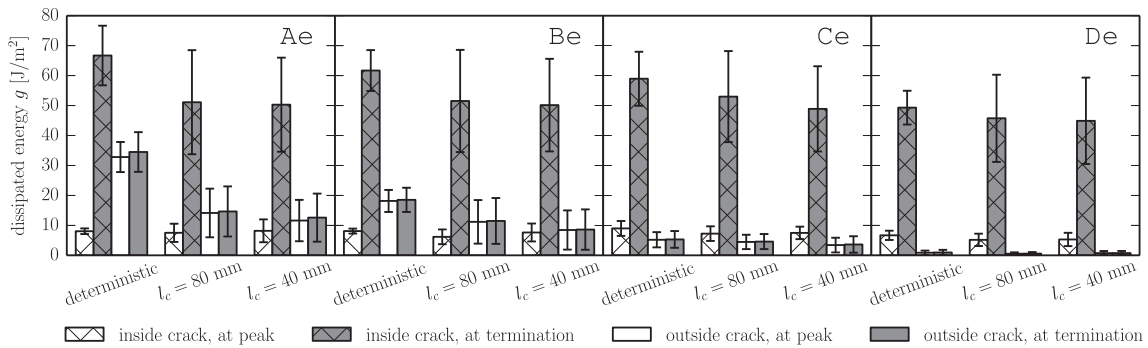


Fig. 11. Energy g calculated in the bottommost 20 mm-thick layer until the peak load was reached or until the termination of the simulation. It is divided into energy dissipated *inside* and *outside* the macrocrack.

this data set with the cohesive crack (or crack band) model can be obtained provided that a bilinear softening with four degrees is used. It was also concluded that this data set cannot be satisfactorily fitted with softening laws of two degrees of freedom, such as the linear softening or Hillerborg's exponential.

A deeper analysis of energy dissipation in unnotched beams is presented in Fig. 11. It shows energy g averaged over two bottommost strips divided into two parts: (i) the energy which was dissipated within ± 15 mm of the macro-crack location, which is labeled as energy *inside* the macro-crack and (ii) the remaining part of the energy, labeled as energy *outside* the macro-crack.

Since localization occurs at peak load, the *outside* energy does not increase much in the postpeak regime. However, it is strongly dependent on applied randomness. It is larger for deterministic models, due to the wide zone of distributed cracking and lower for stochastic models due to the localization of distributed cracking. It seems to be lower for the shorter correlation length, probably because the distributed cracking is even more localized than in the case of the longer correlation length. The *outside* energy is strongly size dependent because the *outside* volume of the material subjected to distributed cracking depends on the beam size as well.

The *inside* energy is also affected by the application of the additional randomness. This is in contradiction with the deep notch results, where the average of the *inside* energy was the same for both deterministic and stochastic models. In unnotched beam geometries, the crack is not forced to initiate at the specific location but is allowed to choose some weakened area along the bottom surface. Since the meso-level strength and fracture energy of rigid-body contacts are positively correlated, the crack that initiates in a weakened material must also dissipate less energy.

In all the foregoing observations the fracture energy is considered as the energy dissipated at one location. What mainly matters for the overall structural response and the deterministic part of size effect is the fracture energy defined as the flux of energy, J , into a propagating fracture process zone, which is defined by Rice's J-integral. For an infinitesimal FPZ, both are equal [39]. But for a finite FPZ, both are proven equal only for steady-state propagation. This is generally not the case here. It would require very large sizes, with FPZ remote from both the notch tip and all boundaries.

7. Summary and conclusions

The enhanced meso-level discrete model has been presented and also employed to reproduce loads and deformations measured in a recent extensive series of experiments on concrete in three-point-bending. An identification procedure of model parameters obtained using a subset of experimental data confirmed the robustness of the model by showing reasonable agreement between simulated and experimental responses for all the data. This verified the predictive capabilities of the model. The model is able to capture size effects on peak load of both, notched and un-notched, specimens; these size effects are in good agreement with the experimental data. After the described simple parameter identification procedure, the model can be used for prediction of behavior of details of concrete structures or obtaining important data for macro-level models that are routinely used in engineering design. The main advantage of the model is its ability to mimic phenomena at mesoscale level that includes gradual transition from distributed damage to strains localization in macro-cracks.

Both deterministic and stochastic versions of the model provide results that suggest dependency of the energy dissipation during fracturing on the specimen size and also notch depth. Nevertheless, this dependency seems to be weak for the studied configurations, especially for large sizes.

The deterministic version of the model (which contains randomness due to the random locations of the largest concrete aggregates) seems to be already sufficient as it reproduces most of the variability measured in the experiments. But it alone cannot capture the Weibull type statistical size effect in large unnotched specimens; for larger specimens or different type of loading (e.g. four point bending or direct tension) the deterministic model would inevitably fail to reproduce the experimental data [17].

The stochastic study with artificially chosen parameters was performed to further investigate the effects of randomness. The following conclusions are in agreement with natural expectations.

- Additional randomness applied to *notched* beams only increases the variability in their strengths and dissipated energies. The mean values of both quantities remain unchanged.
- *Unnotched* beams exhibit lower mean strengths with additional randomness than without it. This is due to the possibility that the crack will initiate from, and grow in, a weak region along the bottom surface.
- The energy dissipation in *unnotched* beams is affected by additional randomness as well. The zone of distributed cracking prior to the peak load is large in the deterministic model, but highly localized into the weaker regions in the stochastic model. This causes an appreciable difference in the dissipated energy between models with and without additional randomness.
- The energy released inside the macro-crack at the bottom surface of *unnotched* beams is lower in the stochastic model than in the deterministic model. This is due to the assumed positive correlation between meso-level strength and fracture energy. The macro-crack prefers to run through weaker regions, where meso-level fracture energy is lower, too.

Acknowledgments

The presented work was initiated during Fulbright research stay of the first author at the Northwestern University under the supervision of prof. Zdeněk P. Bažant. Further financial support received from the Ministry of Education, Youth and Sports of the Czech Republic under projects LH12062 and LO1408 “AdMaS UP - advanced Materials, Structures and Technologies” under the “National Sustainability Programme I” and the Czech Science Foundation under project GA13-03662S is gratefully acknowledged.

Appendix A. Spectral decomposition for EOLE using a grid of nodes

In this section we show how the spectral decomposition of correlation matrix \mathbf{C} can be simplified when using the autocorrelation function defined in Eq. (4). As shown in [43], such a pattern of autocorrelation (fully separable correlation) enables us to greatly simplify the computation of eigenvalues and the associated eigenfunctions (vectors) of the correlation function (matrix). The solution of the eigenvalue problem is a solution to the Fredholm integral equation of the second kind, homogeneous, where the correlation function is the kernel [43].

Let us now assume a discrete case in which the (squared, symmetric) autocorrelation matrix \mathbf{C} of order N is assembled for N grid nodes (random variables). We assume that the grid is formed by N_x nodes along the x -direction, N_y nodes along the y direction and N_z nodes along the z direction. Therefore, the order of the correlation matrix is $N = N_x N_y N_z$. The entries in the correlation matrix are calculated directly from Eq. (4). Each entry in such a correlation matrix can therefore be written as the product of N_d correlations over individual dimensions

$$\mathbf{C}: C_{ij} = \prod_{\text{dim}=x,y,z}^{N_d} \exp\left(-\frac{\|\Delta_{ij,\text{dim}}\|}{l_{c,\text{dim}}}\right)^2 = \rho_x(i,j) \times \rho_y(i,j) \times \rho_z(i,j) \quad i, j = 1, \dots, N \quad (\text{A.1})$$

where indices i, j denote a pair of points (random variables), and N_d is the number of spatial dimensions considered as 3. Therefore, each entry in the matrix is the product of three correlations; the correlation matrix \mathbf{C} can thus be written as a tensor product of three considerably smaller correlation matrices, namely \mathbf{C}_x , \mathbf{C}_y and \mathbf{C}_z

$$\mathbf{C} = \mathbf{C}_x \otimes \mathbf{C}_y \otimes \mathbf{C}_z \quad (\text{A.2})$$

The three matrices \mathbf{C}_x , \mathbf{C}_y and \mathbf{C}_z represent correlation matrices of the three one-dimensional grids along x , y and z directions. This is why the matrices are symmetric positive (semi)definite matrices of orders N_x , N_y and N_z .

We now seek N eigenvalues and eigen-shapes of this matrix (or, the K dominant modes). The problem involved in the simulation of random fields using the Karhunen–Loève expansion is to find such an eigenvalue matrix Λ and the associated orthonormal eigenvectors (columns of) ψ such that

$$\mathbf{C} = \psi \Lambda \psi^T \quad (\text{A.3})$$

The key to simplifying the computation of Λ and ψ lies in the fact that the desired eigenmodes can be obtained as the solution to three smaller problems

$$\Lambda = \Lambda_x \otimes \Lambda_y \otimes \Lambda_z, \quad \psi = \psi_x \otimes \psi_y \otimes \psi_z \quad (\text{A.4})$$

where Λ_x (ψ_x) is the diagonal matrix containing eigenvalues (eigenvectors) of \mathbf{C}_x , $\mathbf{C}_y = \psi_y \Lambda_y \psi_y^T$, etc.

This idea, described in detail for a general number of dimensions in [43], will now be demonstrated using a two-dimensional problem ($N_z = 1$), depicted in Fig. 12. Consider a two-dimensional region covered with a grid of $N = 20$ nodes using $N_x = 5$ and $N_y = 4$ nodal coordinates. For a unidirectional numbering of equidistant nodes along each direction, the correlation matrices \mathbf{C}_x and \mathbf{C}_y are symmetric Toeplitz matrices (diagonal-constant matrices) where the (i, j) th elements depend only on the distance between nodes i and j . Numerical problems involving Toeplitz matrices are typically solved quickly. Specialized algorithms exist for spectral decomposition, see e.g. [2,25,7]. The correlation matrix along the x direction reads

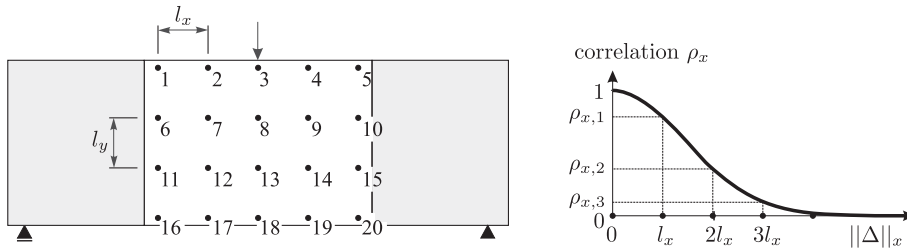


Fig. 12. Left: Example of a two-dimensional grid for the simulation of a random field within a beam. Right: Values of the autocorrelation function along the x-direction.

$$\mathbf{C}_x = \begin{matrix} & \begin{matrix} 1 & 2 & 3 & 4 & 5 \end{matrix} \\ \begin{matrix} 1 \\ 2 \\ 3 \\ 4 \\ 5 \end{matrix} & \begin{pmatrix} 1 & \rho_{x,1} & \rho_{x,2} & \rho_{x,3} & \rho_{x,4} \\ & 1 & \rho_{x,1} & \rho_{x,2} & \rho_{x,3} \\ & & 1 & \rho_{x,1} & \rho_{x,2} \\ & & & 1 & \rho_{x,1} \\ \text{sym.} & & & & 1 \end{pmatrix} \end{matrix} \tag{A.5}$$

and therefore the correlation matrix of the two-dimensional grid can be written as

$$\mathbf{C} = \mathbf{C}_y \otimes \mathbf{C}_x = \begin{matrix} & \begin{matrix} 1 & 6 & 11 & 16 \end{matrix} \\ \begin{matrix} 1 \\ 6 \\ 11 \\ 16 \end{matrix} & \begin{pmatrix} 1 & \rho_{y,1} & \rho_{y,2} & \rho_{y,3} \\ & 1 & \rho_{y,1} & \rho_{y,2} \\ & & 1 & \rho_{y,1} \\ \text{sym.} & & & 1 \end{pmatrix} \otimes \mathbf{C}_x = \begin{matrix} & \begin{matrix} 1-5 & 6-10 & 11-15 & 16-20 \end{matrix} \\ \begin{matrix} 1-5 \\ 6-10 \\ 11-15 \\ 16-20 \end{matrix} & \begin{pmatrix} \mathbf{C}_x & \rho_{y,1}\mathbf{C}_x & \rho_{y,2}\mathbf{C}_x & \rho_{y,3}\mathbf{C}_x \\ & \mathbf{C}_x & \rho_{y,1}\mathbf{C}_x & \rho_{y,2}\mathbf{C}_x \\ & & \mathbf{C}_x & \rho_{y,1}\mathbf{C}_x \\ \text{sym.} & & & \mathbf{C}_x \end{pmatrix} \end{matrix} \tag{A.6}$$

The desired eigenvalue matrix of twenty eigenvalues is constructed as a list of multiplications between all pairs of eigenvalues for each unidirectional grid

$$\mathbf{\Lambda} = \text{diag} \left(\begin{matrix} 1-5 & 6-10 & 11-15 & 16-20 \\ \lambda_{y,1}\Lambda_x & \lambda_{y,2}\Lambda_x & \lambda_{y,3}\Lambda_x & \lambda_{y,4}\Lambda_x \end{matrix} \right) \tag{A.7}$$

and similarly the eigenvector matrix can be constructed as a block matrix

$$\boldsymbol{\psi} = \begin{matrix} & \begin{matrix} 1-5 & 6-10 & 11-15 & 16-20 \end{matrix} \\ \begin{matrix} \psi_y(1,1)\psi_x & \psi_y(1,2)\psi_x & \psi_y(1,3)\psi_x & \psi_y(1,4)\psi_x \\ \psi_y(2,1)\psi_x & \psi_y(2,2)\psi_x & \psi_y(2,3)\psi_x & \psi_y(2,4)\psi_x \\ \psi_y(3,1)\psi_x & \psi_y(3,2)\psi_x & \psi_y(3,3)\psi_x & \psi_y(3,4)\psi_x \\ \psi_y(4,1)\psi_x & \psi_y(4,2)\psi_x & \psi_y(4,3)\psi_x & \psi_y(4,4)\psi_x \end{matrix} \end{matrix} \tag{A.8}$$

Sorting the eigenvalues from the largest to the smallest and simultaneously sorting the columns of $\boldsymbol{\psi}$ enables us to ignore eigenmodes with small eigenvalues.

Such an exploitation of the separable patterns of correlation matrices leads to considerable time and memory savings, and also to increased accuracy. Note that $\mathbf{\Lambda}$ and $\boldsymbol{\psi}$ do not have to be stored in computer memory. For large systems, it is advantageous to save only the source matrices for unidirectional grids (ψ_x , ψ_y , Λ_x and Λ_y) and expand the entries of $\mathbf{\Lambda}$ and $\boldsymbol{\psi}$ during computation. In our meso-level discrete model of bent beams, the grid for autocorrelation length $l = 40$ mm consists of $N = 65.254$ nodes. This grid is constructed using $N_x = 79$, $N_y = 59$ and $N_z = 14$ nodes. Computation of the eigenproblem requires dealing with a correlation matrix of order N ; to store the N eigenvectors in computer memory, one must store $N^2 \approx 4.25 \cdot 10^9$ values. This can not fit into the RAM memory of a common computer. The proposed partitioning enables solution of three problems with matrices of orders $N_x = 79$, $N_y = 59$ and $N_z = 14$. This is considerably easier and the three eigenvector matrices occupy only $N_x^2 + N_y^2 + N_z^2 \approx 9.9 \cdot 10^3$ values. Six orders of magnitude represents a noticeable difference. Combination of this partitioning approach on a grid with EOIE interpolation (Eq. (7)) forms an efficient way of random field generation.

References

[1] Alnaggar M, Cusatis G, Luzzio GD. Lattice discrete particle modeling (LDPM) of alkali silica reaction (ASR) deterioration of concrete structures. *Cem Concr Compos*, 0958-9465 2013;41(0):45–59.
 [2] Andrew AL. Eigenvectors of certain matrices. *Linear Algebra Appl* 1973;7:151–62 [ISSN 0024-3795].

- [3] Bažant ZP, Pang S-D. Activation energy based extreme value statistics and size effect in brittle and quasibrittle fracture. *J Mech Phys Solids* 2007;55(1):91–131 [ISSN 0022-5096].
- [4] Bažant ZP, Tabbara M, Kazemi M, Pijaudier-Cabot G. Random particle model for fracture of aggregate or fiber composites. *J Engng Mech – ASCE* 1990;116(8):1686–705 [ISSN 0733-9399].
- [5] Burt NJ, Dougill JW. Progressive failure in a model heterogeneous medium. *J Engng Mech Div – ASCE* 1977;103(3):365–76 [ISSN 0044-7951].
- [6] Caballero A, López CM, Carol I. 3D meso-structural analysis of concrete specimens under uniaxial tension. *Comput Method Appl M* 2006;195(52):7182–95 [ISSN 0045-7825].
- [7] Coleman JO. A simple FIR-filter interpretation of the extreme eigenvalues of a Toeplitz autocorrelation matrix. *Comput Elect Engng* 2000;26(2):141–9 [ISSN 0045-7906].
- [8] Cusatis G, Bažant ZP, Cedolin L. Confinement-shear lattice model for concrete damage in tension and compression: I. Theory. *J Engng Mech – ASCE* 2003;129(12):1439–48 [ISSN 0733-9399].
- [9] Cusatis G, Bažant ZP, Cedolin L. Confinement-shear lattice CSL model for fracture propagation in concrete. *Comput Method Appl M* 2006;195(52):7154–71 [ISSN 0045-7825].
- [10] Cusatis G, Cedolin L. Two-scale study of concrete fracturing behavior. *Engng Fract Mech* 2007;74(12):3–17 [ISSN 0013-7944].
- [11] Cusatis G, Pelessone D, Mencarelli A. Lattice discrete particle model (LDPM) for failure behavior of concrete. I: Theory. *Cem Concr Comp* 2011;33(9):881–90 [ISSN 0958-9465].
- [12] Eliáš J, Bažant ZP. Fracturing in concrete via lattice-particle model. In: Onate E, Owen D, editors. 2nd International conference on particle-based methods – fundamentals and applications, Barcelona, Spain, 2011.
- [13] Eliáš J, Le J-L. Modeling of mode-I fatigue crack growth in quasibrittle structures under cyclic compression. *Engng Fract Mech* 2012;96:26–36. <http://dx.doi.org/10.1016/j.engfracmech.2012.06.019> [ISSN 0013-7944].
- [14] Eliáš J, Stang H. Lattice modeling of aggregate interlocking in concrete. *Int J Fract* 2012;175:1–11. <http://dx.doi.org/10.1007/s10704-012-9677-3> [ISSN 0376-9429].
- [15] Eliáš J, Vořechovský M, Bažant ZP. Stochastic lattice simulations of flexural failure in concrete beams. In: 8th International conference on fracture mechanics of concrete and concrete structures, Toledo, Spain, 2013.
- [16] Eliáš J, Vořechovský M, Le J-L. Lattice modeling of concrete fracture including material spatial randomness. *Engng Mech* 2013;5:413–26 [ISSN 1802-1484].
- [17] Grassl P, Bažant ZP. Random lattice-particle simulation of statistical size effect in quasi-brittle structures failing at crack initiation. *J Engng Mech – ASCE* 2009;135:85–92 [ISSN 0733-9399].
- [18] Grassl P, Gregoire D, Solano LR, P.-C. Gilles. Meso-scale modelling of the size effect on the fracture process zone of concrete. *Int J Solids Struct* 2013;49(43):1818–27 [ISSN 0020-7683].
- [19] Grassl P, Rempling R. A damage-plasticity interface approach to the meso-scale modelling of concrete subjected to cyclic compressive loading. *Engng Fract Mech* 2008;75(16):4804–18. <http://dx.doi.org/10.1016/j.engfracmech.2008.06.005> [ISSN 0013-7944].
- [20] Grigoriu M. Stochastic systems: uncertainty quantification and propagation. Springer Science & Business Media; 2012 [ISBN 9781447123279].
- [21] Herrmann H, Hansen A, Roux S. Fracture of disordered, elastic lattices in two dimensions. *Phys Rev B* 1989;39(1):637–48 [ISSN 1098-0121].
- [22] Hoover CG, Bažant ZP. Comprehensive concrete fracture tests: size effects of types 1 and 2, crack length effect and postpeak. *Engng Fract Mech* 2013;110:281–9 [ISSN 0013-7944].
- [23] Hoover CG, Bažant ZP. Cohesive crack, size effect, crack band and work-of-fracture models compared to comprehensive concrete fracture tests. *Int J Fract* 2014;87(1):133–43 [ISSN 0376-9429].
- [24] Hoover CG, Bažant ZP, Vorel J, Wendner R, Hubler MH. Comprehensive concrete fracture tests: description and results. *Engng Fract Mech* 2013;114(0):92–103 [ISSN 0013-7944].
- [25] Hu YH, Kung SY. Toeplitz eigensystem solver. *IEEE Trans Acoust Speech Signal Process* 1985;33(4):1264–71 [ISSN 0096-3518].
- [26] Ince R, Arslan A, Karihaloo BL. Lattice modelling of size effect in concrete strength. *Engng Fract Mech* 2003;70(16):2307–20 [ISSN 0013-7944. Size-scale effects].
- [27] Iturriz I, Laciógna G, Carpinteri A. Experimental analysis and truss-like discrete element model simulation of concrete specimens under uniaxial compression. *Engng Fract Mech* 2013;110(0):81–98 [ISSN 0013-7944].
- [28] Jirásek M, Bažant ZP. Macroscopic fracture characteristics of random particle systems. *Int J Fract* 1995;69(3):201–28 [ISSN 0376-9429].
- [29] Jirásek M, Bažant ZP. Particle model for quasibrittle fracture and application to sea ice. *J Engng Mech – ASCE* 1995;121(9):1016–25 [ISSN 0733-9399].
- [30] Jivkov AP, Engelberg DL, Stein R, Petkovski M. Pore space and brittle damage evolution in concrete. *Engng Fract Mech* 2013;110(0):378–95 [ISSN 0013-7944].
- [31] Kang J, Kim K, Lim YM, Bolander JE. Modeling of fiber-reinforced cement composites: discrete representation of fiber pullout. *Int J Solids Struct* 2014;51(10):1970–9 [ISSN 0020-7683].
- [32] Kunieda M, Ogura H, Ueda N, Nakamura H. Tensile fracture process of strain hardening cementitious composites by means of three-dimensional meso-scale analysis. *Cem Concr Comp* 2011;33(9):956–65 [ISSN 0958-9465].
- [33] Le J-L, Bažant ZP. Unified nano-mechanics based probabilistic theory of quasibrittle and brittle structures: II. Fatigue crack growth, lifetime and scaling. *J Mech Phys Solids* 2011;59:1322–37 [ISSN 0022-5096].
- [34] Le J-L, Bažant ZP, Bazant MZ. Unified nano-mechanics based probabilistic theory of quasibrittle and brittle structures: I. Strength, static crack growth, lifetime and scaling. *J Mech Phys Solids* 2011;59(7):1291–321 [ISSN 0022-5096].
- [35] Li CC, Der Kiureghian A. Optimal discretization of random fields. *J Engng Mech – ASCE* 1993;119(6):1136–54 [ISSN 0733-9399].
- [36] Li HS, Lü ZZ, Yuan XK. Nataf transformation based point estimate method. *Chin Sci Bull* 2008;53(17):2586–92.
- [37] Man H-K, van Mier JGM. Influence of particle density on 3D size effects in the fracture of (numerical) concrete. *Mech Mater* 2008;40(6):470–86 [ISSN 0167-6636].
- [38] Mungule M, Raghuprasad BK, Muralidhara S. Fracture studies on 3D geometrically similar beams. *Engng Fract Mech* 2013;98(0):407–22 [ISSN 0013-7944].
- [39] Rice J. Mathematical analysis in the mechanics of fracture. In: Liebowitz H, editor. Fracture: an advanced treatise, vol. 2. Academic Press; 1968. p. 191–311.
- [40] Šavija B, Pacheco J, Schlangen E. Lattice modeling of chloride diffusion in sound and cracked concrete. *Cem Concr Comp* 2013;42(0):30–40 [ISSN 0958-9465].
- [41] Schlangen E, Garbocci EJ. Fracture simulations of concrete using lattice models: computational aspects. *Engng Fract Mech* 1997;57(2–3):319–32 [ISSN 0013-7944].
- [42] van Mier JGM. Concrete fracture: a multiscale approach. CRC Press; 2013 [ISBN 9781466554702].
- [43] Vořechovský M. Simulation of simply cross correlated random fields by series expansion methods. *Struct Saf* 2008;30(4):337–63 [ISSN 0167-4730].
- [44] Vořechovský M, Novák D. Correlation control in small-sample monte carlo type simulations I: A simulated annealing approach. *Probabilist Engng Mech* 2009;24(3):452–62 [ISSN 0266-8920].
- [45] Vořechovský M, Sadílek V. Computational modeling of size effects in concrete specimens under uniaxial tension. *Int J Fract* 2008;154(1–2):27–49 [ISSN 0376-9429].
- [46] Wendner R, Vorel J, Smith J, Hoover CG, Bažant ZP, Cusatis G. Characterization of concrete failure behavior: a comprehensive experimental database for the calibration and validation of concrete models. *Mat Struct* 2014:1–24. <http://dx.doi.org/10.1617/s11527-014-0426-0> [ISSN 1359-5997].
- [47] Zubelewicz A, Bažant ZP. Interface element modeling of fracture in aggregate composites. *J Engng Mech – ASCE* 1987;113(11):1619–30 [ISSN 0733-9399].